



Oxygen Permeable Membrane Hot Paper

How to cite: *Angew. Chem. Int. Ed.* **2023**, *62*, e202210485

International Edition: doi.org/10.1002/anie.202210485

German Edition: doi.org/10.1002/ange.202210485

Multilayered Ceramic Membrane with Ion Conducting Thin Layer Induced by Interface Reaction for Stable Hydrogen Production

Guanghu He, Qianqian Lan, Mengke Liu, Guixuan Wu, Rafal E. Dunin-Borkowski, and Heqing Jiang*

Abstract: Conventional methods for fabricating multilayered ceramic membranes with ion conducting dense thin layers are often cumbersome, costly, and limited by poor adhesion between layers. Inspired by the architectural structure of the rooted grasses in soil, here, we report an interface-reaction-induced reassembly approach for the direct fabrication of $\text{Ce}_{0.9}\text{Gd}_{0.1}\text{O}_{2-\delta}$ (CGO) thin layers rooted in the parent multilayered ceramic membranes by only one firing step. The CGO dense layers are very thin, and adhered strongly to the parent support layer, ensuring low ionic transport resistance and structural integrity of the multilayered membranes. When using as an oxygen permeable membrane for upgrading fossil-fuel-derived hydrogen, it shows very long durability in harsh conditions containing H_2O , CH_4 , H_2 , CO_2 and H_2S . Furthermore, our approach is highly scalable and applicable to a wide variety of ion conducting thin layers, including $\text{Y}_{0.08}\text{Zr}_{0.92}\text{O}_{2-\delta}$, $\text{Ce}_{0.9}\text{Sm}_{0.1}\text{O}_{2-\delta}$ and $\text{Ce}_{0.9}\text{Pr}_{0.1}\text{O}_{2-\delta}$.

Introduction

Ceramic membranes consisting of ion conducting dense layers and porous support layers are essential platforms for solid state electrochemical devices, gas separation membranes and sensor.^[1] Depending on the species of mobile ions in the dense layer of interest, multilayered ceramic membranes can range from oxygen ion conductors such as

$\text{Ce}_{0.9}\text{Gd}_{0.1}\text{O}_{2-\delta}$ (CGO) and $\text{Y}_{0.08}\text{Zr}_{0.92}\text{O}_{2-\delta}$ (YSZ) to mixed ionic-electronic conductors such as $\text{Ba}_{0.5}\text{Sr}_{0.5}\text{Co}_{0.8}\text{Fe}_{0.2}\text{O}_{3-\delta}$. For the applications in solid oxide fuel cells (SOFCs),^[2] electrolysis cells (SOECs)^[3] or oxygen permeable membrane reactors,^[4] it is essential that the ion conducting dense layers should be as thin as possible to minimize ionic transport resistance. For example, in a ceramic fuel cell, a 15- μm -thick $\text{Ce}_{0.8}\text{Sm}_{0.2}\text{O}_{2-\delta}$ dense layer was deposited on a 800- μm -thick $\text{BaZr}_{0.1}\text{Ce}_{0.7}\text{Y}_{0.1}\text{Yb}_{0.1}\text{O}_{3-\delta}$ porous support layer.^[5] Also, a 20- μm -thick $\text{Ba}_{0.95}\text{La}_{0.05}\text{FeO}_{3-\delta}$ dense layer on a 1400- μm -thick porous support layer was employed as oxygen permeable membranes.^[6]

Multilayered ceramic membranes are typically fabricated using layer-by-layer deposition strategy.^[7] As shown in Figure 1a, a serial procedure is normally required, starting from the initial preparation of porous support layer, followed by the deposition of ion conducting dense thin layer on the porous support, and subsequential multiple drying-sintering steps. However, most of these methods are time-consuming, energy-intensive and lack of fabrication flexibility. Furthermore, the thicknesses of the dense thin layers are commonly between 10 and 1000 μm ,^[8] resulting in high ionic transport resistance. Although physical vapor deposition techniques can reduce this thickness to submicron meter (100–500 nm), the scaling of these techniques remains problematic because of their relatively slow deposition rates and high investment costs.^[9] In addition, the deposited thin layers often delaminate from the support layers during co-sintering because of the thermal expansion mismatch between different layers^[10] (Figure 1a). Despite several strategies (e.g., applying a load during co-sintering,^[11] regulating the microstructure of the porous layer^[12] or artificially interposing an interlayer^[5]) have been proposed to improve the layer-layer adhesion, these methods remain empirical, leading to poor reproducibility. Thus, an efficient approach to decrease the thickness of ion conducting dense layer and significantly enhance the interlaminar adhesion in multilayered ceramic membranes is in great demand.^[2]

In this work, we depart from traditional approaches for fabricating the multilayered ceramic membranes. Inspired by the architectural structure of the rooted grasses in soil (Figure 1b), we develop an interface-reaction-induced reassembly approach to the fabrication of a three-layered ceramic membrane comprising a porous support layer, an intermediate parent layer and a derived surface thin layer rooted in its parent layer, directly resulting from a single-step sintering of dual-phase ceramic precursors consisting of fluorite-type oxides (e.g., $\text{Ce}_{0.9}\text{Gd}_{0.1}\text{O}_{2-\delta}$ or $\text{Y}_{0.08}\text{Zr}_{0.92}\text{O}_{2-\delta}$)

[*] Dr. G. He, M. Liu, Prof. Dr. H. Jiang
Qingdao New Energy Shandong Laboratory, Qingdao Institute of Bioenergy and Bioprocess Technology
Chinese Academy of Sciences
189 Songling Road, Qingdao, 266101 (China)
E-mail: jianghq@qibebt.ac.cn

Dr. G. He, Prof. Dr. H. Jiang
Shandong Energy Institute
189 Songling Road, Qingdao, 266101 (China)

Dr. Q. Lan, Prof. Dr. R. E. Dunin-Borkowski
Ernst Ruska-Centre for Microscopy and Spectroscopy with Electrons and Peter Grünberg Institute 5 (PGI-5), Forschungszentrum Jülich
Wilhelm-Johnen-Straße, 52425 Jülich (Germany)

Dr. G. Wu
GTT-Technologies
Kaiserstraße 103, 52134 Herzogenrath (Germany)

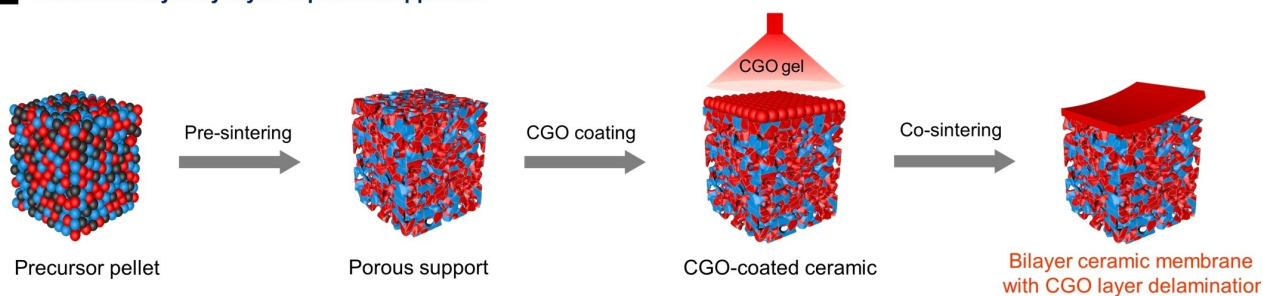
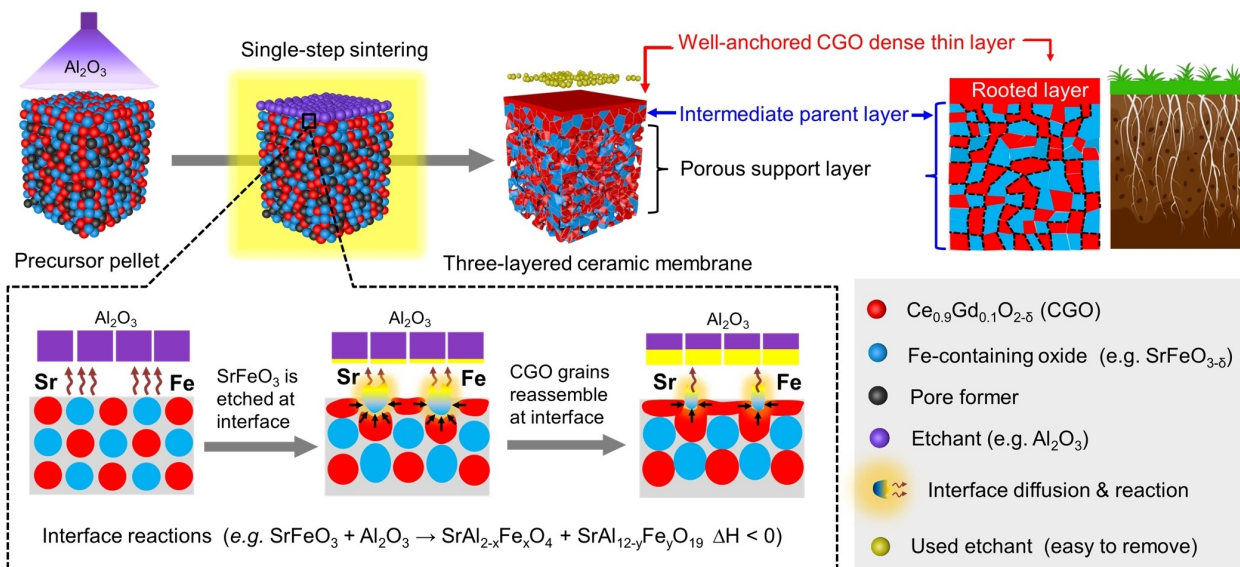
a Traditional layer-by-layer deposition approach**b** Interface-reaction-induced reassembly approach

Figure 1. Schematic illustration of the fabrication of a multilayered ceramic membrane with an ion conducting dense layer by a) traditional layer-by-layer deposition; b) interface-reaction-induced reassembly.

and Fe-containing oxides (e.g., SrFeO_{3-δ} or NiFe₂O₄). In this approach, Al₂O₃, thermally compatible with fluorite-type oxides,^[13] is deliberately chosen as a surface etchant because it can react with Fe-containing oxides to produce aluminates.^[14] As shown in Figure 1b, at high temperatures, the surface SrFeO₃ grains in the CGO-SrFeO₃ dual-phase ceramic pellet are selectively etched by Al₂O₃ via interface reactions at high temperatures (e.g., SrFeO_{3-δ}+Al₂O₃→SrAl_{2-x}Fe_xO₄+SrAl_{12-y}Fe_yO₁₉, ΔH<0),^[14] producing reaction enthalpy (Figure S1). The heat released by the interface reactions is expected to increase the local temperature for accelerating SrFeO₃ erosion and simultaneously driving the reassembly of the surface isolated CGO grains into a dense layer that will separate the underneath SrFeO₃ grains from the surface Al₂O₃. Thus the interface reactions will be automatically cut off, avoiding the continuous thickness increase of the CGO dense layer. Interestingly, the *in situ* derived CGO surface thin layer is well rooted in its parent layer (*i.e.*, the intermediate layer), creating strong layer-layer adhesion. Meanwhile, the underlying porous layer is formed after burning-out of the pore former, which is

deliberately added during the fabrication of the precursor pellet. Notably, this new approach for the fabrication of a three-layered ceramic membrane is straightforward with only a single sintering step, and therein the CGO thin layer is intensely adhered to the parent dual-phase layer, ensuring the structural integrity of the multilayered ceramic.

Results and Discussion

To demonstrate the feasibility of this approach, CGO and Gd_{0.1}Sr_{0.9}Fe_{0.9}Ti_{0.1}O_{3-δ} (GSFT) are specifically used as starting dual-phase precursors. Colloidal Al₂O₃ was first applied onto the surface of a CGO-GSFT dual-phase green pellet by a drop-coating method. As expected, the CGO grains in contact with the Al₂O₃ particles gathered to form a dense layer after sintering (Figure S2). In another simpler experiment, a CGO-GSFT green compact was sintered directly on a flat Al₂O₃ substrate. After single-step sintering, a flat three-layered ceramic membrane was obtained, consisting of a CGO thin (≈2.5 μm) layer that was well anchored to its

intermediate parent layer and a thick porous support layer (Figures 2a, b and Figures S3–S4). Therein the intermediate layer and the porous layer retained their initial CGO-GSFT composite phases, whereas only fluorite-structured CGO was detected for the thin layer contacting with the Al_2O_3 substrate (Figure 2c), indicating interfacial reassembly of the (CGO-GSFT)/ Al_2O_3 system during sintering. Different from the two sets of XRD peaks of the porous layer, the diffraction peaks of the CGO thin layer can be indexed only to $\text{Ce}_{0.9}\text{Gd}_{0.1}\text{O}_{1.95}$ (JCPDS No. 75-0161).^[15] Adhesion of the CGO thin layer to the CGO-GSFT parent layer was assessed by scratch tests, and a high critical load (L_c) of up to 40 N was obtained before the spallation of the rooted layer, as shown in Figure 2d. Compared to magnetron-sputtered or sol-gel-deposited CeO_{2-x} coatings, for which

the critical loads are only 22.4 and 28.8 N,^[16] respectively, the interface-reaction-induced CGO layer in this work exhibits much stronger adhesion to the CGO-GSFT parent layer, avoiding warpage and/or delamination of the CGO thin layer^[17] and maintaining the structural integrity of the three-layered ceramic membrane. Furthermore, by adjusting the CGO/GSFT ratio of the precursor, sintering temperature and dwell time (Figures S5–S7), the thickness of the CGO layer in the layered ceramic membrane could be further reduced to $\approx 1.2\ \mu\text{m}$, overcoming the restrictions of traditional approaches for the fabrication of multilayered ceramic membranes with CGO dense layers for SOFC/SOEC use (Figure 2e).^[7c, 10b, 18] It is worth noting that the CGO-GSFT intermediate layer can conduct both electrons

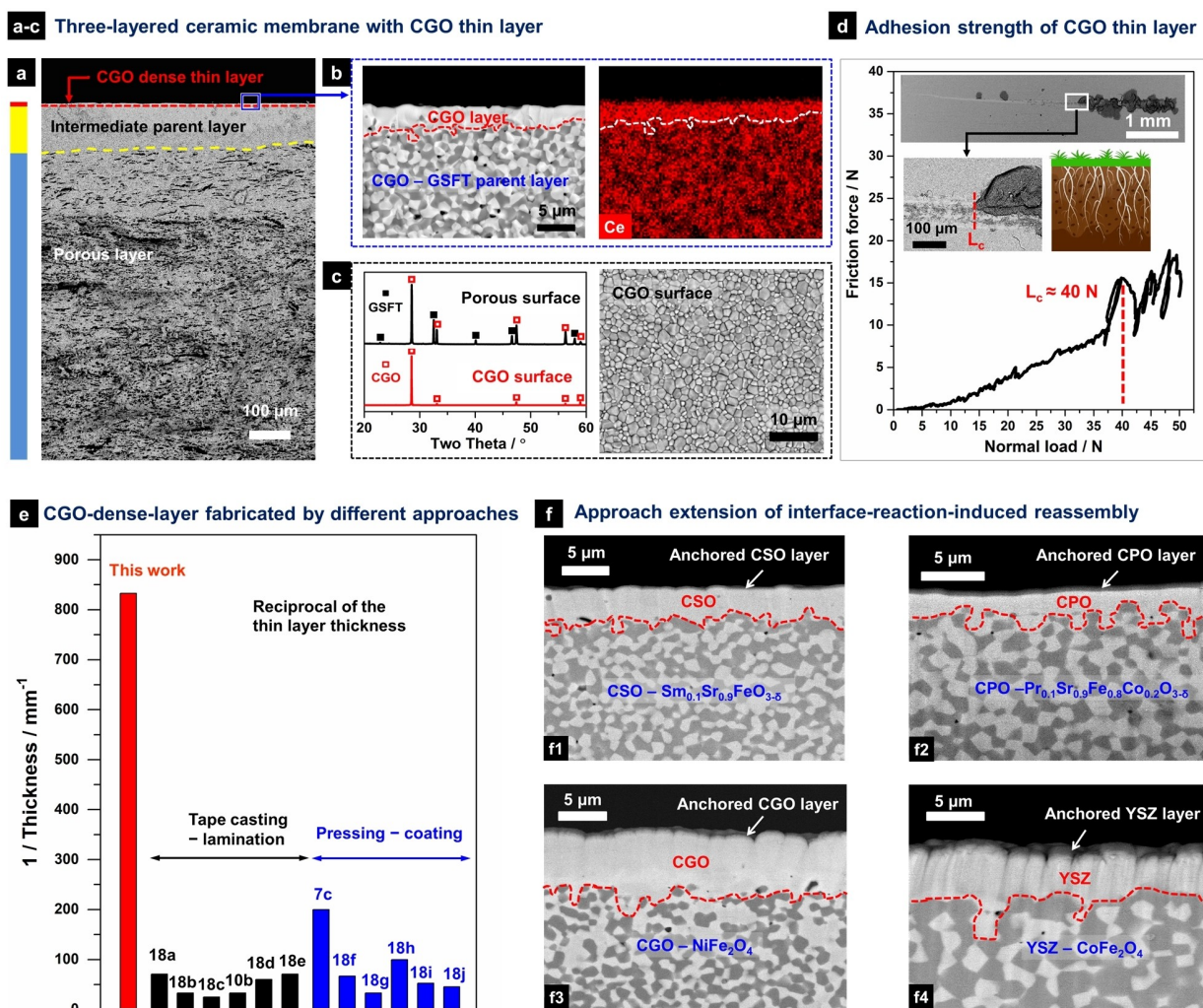


Figure 2. Multilayered ceramic membranes with interface-reaction-induced $\text{Ce}_{0.9}\text{M}_{0.1}\text{O}_{2-\delta}$ (CMO, M = Gd, Sm, Pr) or $\text{Y}_{0.08}\text{Zr}_{0.92}\text{O}_{2-\delta}$ (YSZ) dense thin layers. a) Cross-sectional BSE image of three-layered ceramic membrane; b) BSE image and Ce elemental analysis of the CGO thin layer, which is well rooted in the intermediate layer, recorded from the marked region in (a); c) XRD and BSE of the CGO and porous layers of the three-layered ceramic membrane in (a). d) Scratch adhesion behavior of the CGO thin layer on the CGO-GSFT parent layer. The inset shows BSE images of the scratch areas and an illustration of rooted grasses in soil. e) Reciprocal of CGO-dense-layer thickness fabricated by interface-reaction-induced reassembly, tape casting-lamination, and pressing-coating approaches. f) BSE images of four multilayered ceramic membranes with f1) CSO, f2) CPO, f3) YSZ and f4) CGO thin layers, respectively.

and ions, thus being a suitable mixed conductor for fuel cell electrodes and oxygen permeable membranes.

Remarkably, this simple approach can be readily extended to fabricate the other ten different layered ceramic membranes with $\text{Ce}_{0.9}\text{M}_{0.1}\text{O}_{2-\delta}$ (CMO, M=Gd, Sm, Pr) or $\text{Y}_{0.08}\text{Zr}_{0.92}\text{O}_{2-\delta}$ (YSZ) thin layers from dual-phase systems consisting of fluorite-type oxides (e.g., CMO or YSZ) and Fe-containing oxides (e.g., $\text{La}_{0.1}\text{Sr}_{0.9}\text{FeO}_{3-\delta}$, $\text{SrFe}_{0.5}\text{Ce}_{0.5}\text{O}_{3-\delta}$, NiFe_2O_4 or CoFe_2O_4 etc.), as shown in Table S1, and in the form of back-scattered electron (BSE) images (Figure 2f), and the corresponding X-ray diffraction (XRD) (Figure 2f), and the corresponding X-ray diffraction (XRD) and energy-dispersive X-ray spectroscopy (EDX) analyses (Figures S8–S13). These multilayered ceramic membranes with CMO or YSZ thin layers will be of high interest as ionic conductors for applications in oxygen permeable membranes, SOFC/SOECs and oxygen sensors. Another remarkable finding is that this approach also enables the scalable fabrication of large-area, flat multilayer sheets. BSE images (Figure S14) show the morphology and composition of an approximately $5 \times 5 \text{ cm}^2$ flat sample, in which the CGO layer is very thin (\approx

$2 \mu\text{m}$), dense and well-adhered to the parent support layer. No defects or delamination are observed for the CGO thin layer, highlighting the scalability of this approach and its potential for practical applications.

The CGO thin layer in the CGO/(CGO-GSFT) layered ceramic membrane and the used Al_2O_3 substrate (as the etchant) were characterized to understand the interface-reaction-induced reassembly process during sintering. Transmission electron micrographs, its Fast Fourier Transform and a selected area electron diffraction pattern (Figure 3a–c) indicate that the CGO layer in the layered ceramic membrane is fully crystallized and is in the cubic fluorite phase. EDX elemental maps (Figure 3d) and line scan profiles (Figure S15) show that Ce, Gd and O are distributed homogeneously, while Sr, Fe, Ti and Al are below the detection limit. This reveals no observable elemental diffusion between CGO and GSFT or between CGO and Al_2O_3 during sintering,^[13] as also evidenced by XRD analysis of the co-fired CGO-GSFT and CGO- Al_2O_3 powders (Figure S16). Furthermore, an EDX line scan across CGO and

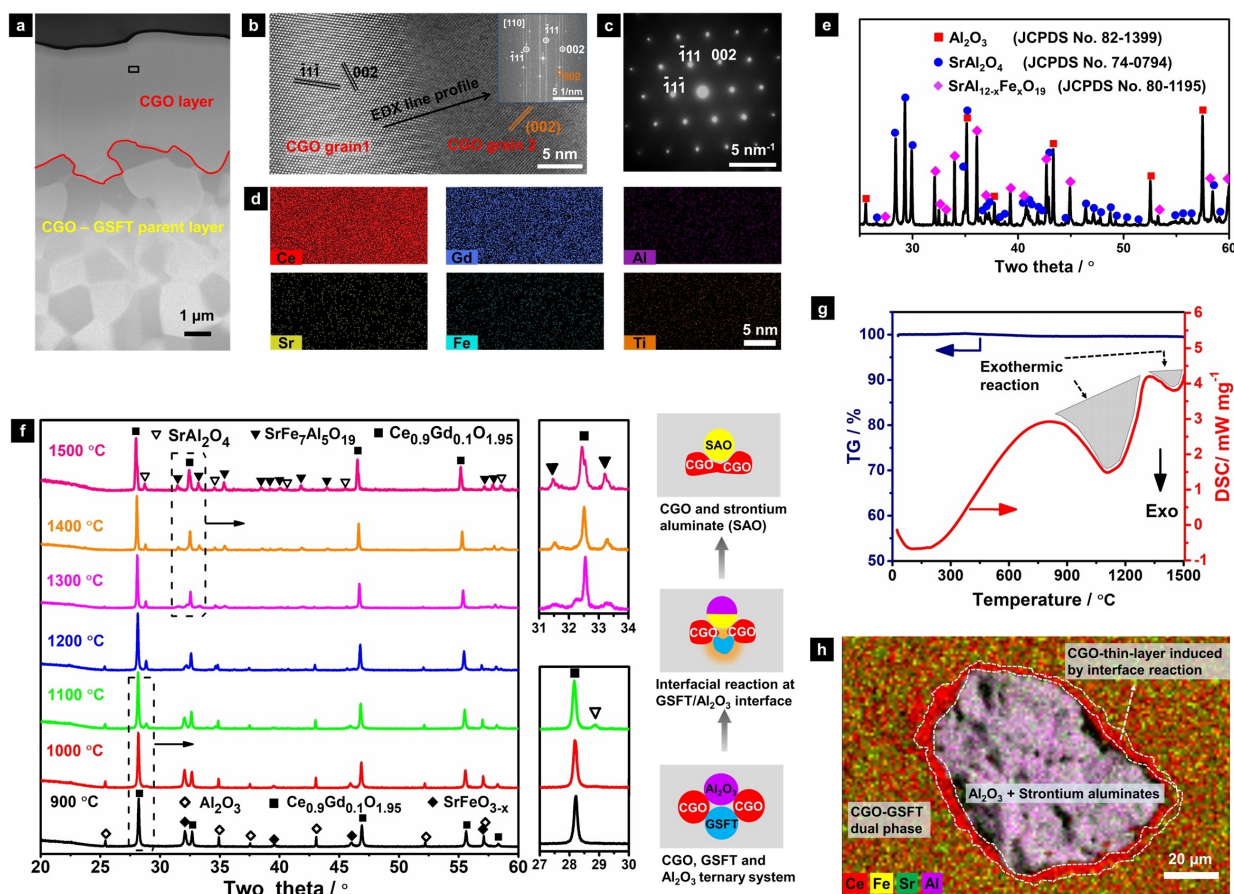


Figure 3. Characterization of CGO-GSFT- Al_2O_3 system and formation mechanism of the CGO dense thin layers in multilayered ceramic membranes. a) Low magnification cross-sectional high-angle annular dark field scanning transmission electron microscopy (HAADF STEM) image of the CGO/(CGO-GSFT) layers. b) Atomically-resolved HAADF STEM image of an interface between two CGO grains recorded from the marked region in (a). The inset shows its Fourier transform. c) Selected area electron diffraction pattern of the CGO grain. d) Elemental maps of Ce, Gd, Al, Sr, Fe and Ti, respectively, obtained from the same region in (b). e) XRD pattern of the used Al_2O_3 substrate surface. f) In situ X-ray diffraction of CGO-GSFT- Al_2O_3 oxides collected upon heating from 900 to 1500 °C in ambient atmosphere, alongside a sketch of the phase composition change of Al_2O_3 /GSFT/CGO composite with increasing temperature. g) TGA and DSC spectra of the GSFT- Al_2O_3 oxides. h) EDX elemental map of Ce, Sr, Fe and Al around an Al_2O_3 particle in CGO-GSFT oxides after sintering at 1450 °C.

GSFT grains near CGO thin layer (Figure S17) indicates that no obvious Al, originating from Al_2O_3 , could diffuse through the CGO dense layer and then reach the underneath GSFT grains at high temperature. In contrast, Sr and Fe diffusion from the GSFT grains to Al_2O_3 take place (Figure S18), leading to interface reactions to produce porous deposit of strontium aluminates (e.g., SrAl_2O_4 ^[19] and $\text{SrAl}_{12-x}\text{Fe}_x\text{O}_{19}$ ^[20]) on the Al_2O_3 ^[21] surface (Figure 3e). The results suggest that CGO at the (CGO-GSFT)/ Al_2O_3 interface was chemically stable, while Al_2O_3 can interfacially etch GSFT grains at the CGO-GSFT surface. The remaining isolated CGO grains at the etched surface reassemble into a dense thin layer that will immediately cut off Sr/Fe diffusion and stop the interface reactions, avoiding the continuous thickness increase of the CGO dense layer. The driving force for the reassembly of isolated CGO grains will be discussed in the following section.

In order to further understand the interface reactions between Al_2O_3 and GSFT, *in situ* high temperature XRD measurements of granular composite oxides CGO-GSFT- Al_2O_3 were carried out. Figure 3f and Figure S19 show that CGO maintains its cubic structure from room temperature to 1500 °C and has good thermal and chemical compatibility with both Al_2O_3 and GSFT at high temperature, matching well with the mentioned *ex situ* XRD results (Figure S16). However, the diffraction intensities of Al_2O_3 (e.g., $2\theta = 25.4^\circ$) and GSFT (e.g., $2\theta = 32.1^\circ$) become weak above 1000 °C and then disappear at 1300 °C. Simultaneously, new diffraction peaks (e.g., $2\theta = 28.8^\circ$, 31.5°), which can be assigned to SrAl_2O_4 (JCPDS No. 31-1336)^[22] and $\text{SrFe}_7\text{Al}_5\text{O}_{19}$ (JCPDS No. 71-1027),^[23] appear above 1000 °C and gradually increase as the temperature rises to 1500 °C. These observations indicate that Al_2O_3 was thermally compatible with CGO, while reacting with GSFT to produce aluminates ($\text{Al}_2\text{O}_3 + \text{GSFT} \rightarrow \text{SrAl}_2\text{O}_4 + \text{SrFe}_7\text{Al}_5\text{O}_{19}$) at high temperature. This is further supported by thermal gravimetric analysis (TGA) and differential scanning calorimetry (DSC) spectra of Al_2O_3 -GSFT oxides (Figure 3g), presenting two broad exothermic peaks observed between 900 and 1500 °C without detectable weight loss. The heat released by the interface reactions is expected to increase the local temperature for driving the reassembly of surface isolated CGO grains into a dense thin layer. Such interfacial reassembly can be supported by the following observation. As shown in Figure 3h and Figure S20, once deliberately adding few Al_2O_3 granules into a CGO-GSFT green compact, it was found that the Al_2O_3 granule in the compact was surrounded by a CGO dense layer rather than GSFT and/or CGO-GSFT grains after a single-step sintering at 1450 °C.

It should be noted that the pressed CGO-GSFT green membrane was porous with a rough surface, while the fresh Al_2O_3 substrate was dense with a relatively smooth surface (Figure S21). Thus, the contact gaps between the CGO-GSFT green membrane and the Al_2O_3 substrate might provide the space for the strontium aluminates produced at the interface. After sintering was finished, the (CGO-GSFT)/CGO layered membrane can be easily separated from the Al_2O_3 substrate (Supporting Information Video 1).

This was probably attributed to the formation of porous deposit of strontium aluminates with very small amount between the ceramic membrane and Al_2O_3 substrate (Figure S21), which reduce the contact area and thus weaken adhesion between the CGO layer and the Al_2O_3 substrate.^[24]

The *in situ* and *ex situ* characterization techniques described above for a representative CGO-GSFT- Al_2O_3 system clearly demonstrated that, at high temperature, GSFT at the interface was chemically etched by Al_2O_3 associated with Sr/Fe diffusion and exothermic interface reactions. CGO was thermally and chemically stable in the composite system. Based on these observations, the formation mechanism of a CGO dense thin layer in a multilayered ceramic membrane from CGO-GSFT raw precursors can be inferred. Upon heating a CGO-GSFT green compact on an Al_2O_3 substrate, Sr and Fe start to diffuse from the GSFT to the Al_2O_3 at the interface, accompanied with the exothermic interface reactions that generate porous strontium aluminates on the surface of the dense Al_2O_3 substrate, leading to the gradual erosion of the surface GSFT grains in the CGO-GSFT compact. Also, the heat from the interface reactions increases the local temperature for driving the reassembly and growth of surface isolated CGO grains. It should be noted that all the processes including strontium aluminates generation, surface GSFT erosion and surface CGO reassembly do happen simultaneously and are highly correlated. With the increase of temperature and the extension of sintering time (e.g. 1450 °C for 10 hours), the interface reactions between GSFT and Al_2O_3 are being promoted so that the surface GSFT is increasingly etched, meanwhile the surface CGO grains continue to grow and reassemble until the formation of a fully connected CGO dense layer that will immediately cut off Sr/Fe diffusion and stop the interface reactions. Interestingly, the continuous thickness increase is automatically suppressed in this technique. This mechanism can also explain the formation of the aforementioned various CMO and YSZ dense thin layers rooted in the layered ceramic membranes from initial composite oxides (Figure 2f and Figures S8–S13).

Recently, significant efforts have been made to obtain pure hydrogen from industrial by-product hydrogen, for example, coke oven gas (COG) containing H_2 , CH_4 , CO_2 , CO and H_2S .^[25] In addition to H_2 -permeable molecular sieve membranes and Pd-based membranes,^[26] mixed ionic and electronic conducting (MIEC) ceramic membranes with 100 % oxygen permeation selectivity have been proposed to purify raw hydrogen with the assistance of water splitting.^[27] At elevated temperatures, water and raw hydrogen are fed to opposite sides of an oxygen permeable dense membrane. H_2O is dissociated into H_2 and oxygen on one side of the membrane, the oxygen can transport as oxygen ions (O^{2-}) through the membrane and then consumed by raw hydrogen on the other side. Thus, water dissociation can proceed continuously and pure H_2 can be obtained after steam condensation. The obtained H_2 is essentially free of impurities such as CO and H_2S which are two critical poisoning species in fuel cells. The potential applicability of oxygen permeable ceramic membranes for upgrading fossil-fuel-derived hydrogen relies on their permeability and long-

term durability under practical conditions (e.g., with feed streams containing H_2 , CH_4 , CO_2 , CO and H_2S).^[28] Considering CGO displays MIEC and good chemical stability in reducing atmospheres, we evaluated the oxygen permeable performance of an interface-reaction-induced CGO/(CGO-GSFT) multilayered ceramic membrane in a range of harsh operational conditions.

Bi-layered CGO/(CGO-GSFT) ceramic membranes were first treated at 750 °C in pure CO_2 or the mixture (wet H_2) of 3 vol. % H_2O –97 vol. % H_2 for 500 hours. The surface morphologies and crystal structures of the layered membranes were preserved in both cases (Figure 4a, Figure S22), confirming that multilayered membranes with protecting CGO thin layers have excellent resistance towards CO_2 and wet H_2 atmospheres. In contrast, the referenced symmetric CGO-GSFT membranes without protecting CGO thin layer were severely corroded after treatment in the same atmospheres (Figure 4b), because of the poor chemical stability of GSFT grains in either CO_2 or wet H_2 atmospheres. The same observations were reported for other Fe-containing MIEC membranes including $\text{BaFe}_{0.8}\text{Nb}_{0.2}\text{O}_{3-\delta}$ ^[29] and $\text{Sm}_{0.15}\text{Ce}_{0.85}\text{O}_{1.925}$ – $\text{Sm}_{0.6}\text{Sr}_{0.4}\text{Al}_{0.3}\text{Fe}_{0.7}\text{O}_{3-\delta}$ ^[30] in which the structure degradations were attributed to the formation of strontium carbonate in CO_2 or the over-reduction of Fe ions

in reducing atmospheres. The excellent stability of CGO/(CGO-GSFT) layered membranes in CO_2 and wet H_2 atmospheres therefore benefits from the presence of the CGO dense thin layers.

Oxygen permeation tests were carried out for the bi-layered CGO/(CGO-GSFT) ceramic membrane in six different operating conditions. As shown in Figure 4c, the CGO dense thin layer with a loading catalyst was subjected to low p_{O_2} atmospheres (He, CO_2 , CH_4 , CH_4 - H_2 - CO_2 - N_2 , and CH_4 - H_2 - CO_2 - N_2 with 37 ppm H_2S in sequence), while the other side of the membrane was exposed to relatively high p_{O_2} atmospheres (synthetic air, H_2O -Ar, and H_2O -He in sequence). When changing the operating conditions from air/ CO_2 to air/ CH_4 , the oxygen permeation flux ($J(\text{O}_2)$) of the bi-layered membrane increased rapidly from 0.015 to $0.52 \text{ cm}^3 \text{ min}^{-1} \text{ cm}^{-2}$. This should be relevant to the environment-induced-reduction of Ce^{4+} to Ce^{3+} in the CGO thin layer in the CH_4 atmosphere,^[31] changing the protecting CGO layer from an oxygen-ion conductor to a mixed oxygen ionic and electronic conductor. As the reduction further proceeded, the mixed conductivity of the CGO thin layer increased gradually, resulting in a continuous increase of the permeation flux to $0.58 \text{ cm}^3 \text{ min}^{-1} \text{ cm}^{-2}$. Afterwards, the feed gas was changed from synthetic air to diluted steam,

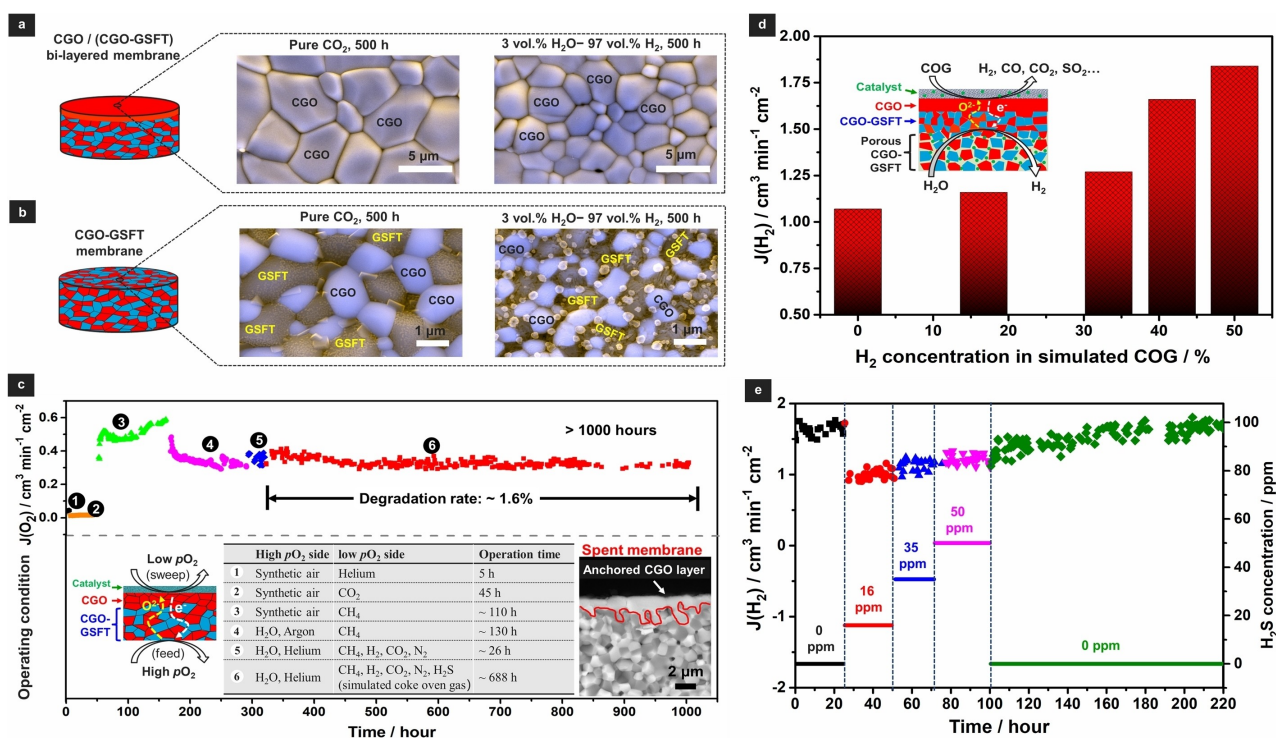


Figure 4. Membrane performance of multilayered ceramics with CGO thin layers in harsh conditions. a) Mixed BSE and SE images of the CGO layer of the CGO/(CGO-GSFT) layered ceramic membranes treated at 750 °C in pure CO_2 or 3 vol. % H_2O –97 vol. % H_2 atmospheres for 500 hours each. b) Mixed BSE and SE images of the CGO-GSFT membrane surfaces treated at 750 °C in pure CO_2 or 3 vol. % H_2O –97 vol. % H_2 atmospheres for 500 hours. c) Illustration of > 1000 hour long-term stability of CGO/(CGO-GSFT) oxygen permeable membrane at 925 °C under six different service conditions. The insets show (i) a schematic diagram of oxygen permeation through a catalytic multilayered membrane; (ii) a table showing the operation conditions of the layered membrane; and (iii) a BSE image of the cross-section of the spent layered membrane. d) Effects of H_2 concentration and e) H_2S concentration in a simulated COG stream on hydrogen production rate from water splitting by using a CGO/(CGO-GSFT)/p(CGO-GSFT) three-layered membrane reactor at 925 °C. The inset in (d) shows a schematic diagram of hydrogen production from water splitting driven by COG oxidation.

achieving the coupling of water splitting with the oxidation of methane in the membrane reactor to simultaneously produce hydrogen and synthesis gas (a mixture of H_2 and CO), similar to the concept in our previous works.^[32] Before the test was intentionally stopped, the membrane had been operated continuously and steadily for an approximately 850-hour period in which multiple reactions were coupled on opposite sides of the membrane. In particular, the $J(O_2)$ in an $(H_2O-He)/(CH_4-H_2-CO_2-N_2-H_2S)$ gradient stayed at $\approx 0.32 \text{ cm}^3 \text{ min}^{-1} \text{ cm}^{-2}$ for 688 hours with a degradation rate of only 1.6 %, as compared to a significant 80 % degradation after 480-hour operation in a typical Fe-based ceramic membrane under sulfur-containing atmosphere.^[33] These results highlight the excellent chemical stability and good oxygen permeability of the CGO/(CGO-GSFT) membrane in harsh conditions containing CH_4 , H_2 , CO_2 and H_2S , which are the main constituents of coke oven gas (COG) in the steel industry. After this long-term test, the structural integrity of the CGO/(CGO-GSFT) layered membrane was retained (the third inset in Figure 4d), again emphasizing the intense adhesion of the thin CGO layer to the parent support layer. In addition, the analyses of phase composition and morphology of the spent membrane indicate that the parent CGO-GSFT layer was protected from the corrosive gases by the CGO dense thin layer (Figure S23).

Taken together, the referenced symmetric CGO-GSFT oxygen permeable membranes tend to be reduced or carbonated in the reducing or CO_2 atmospheres, making them unsuitable for the intended industrial applications, although they show high oxygen permeation fluxes ($> 1 \text{ cm}^3 \text{ min}^{-1} \text{ cm}^{-2}$).^[34] The stability can be significantly improved by introducing a CGO dense thin layer on the membrane surface through the interface-reaction-induced reassembly approach, forming an asymmetric bi-layered membrane (i.e. CGO/(CGO-GSFT)). Benefiting from the CGO dense thin layer with excellent chemical stability and mixed conductivity, the multilayered membrane can be operated with a steady oxygen permeation flux for > 1000 hours under harsh operating conditions containing CH_4 , H_2 , CO_2 and H_2S , therefore is expected to be a promising candidate for upgrading the fossil-fuel-derived hydrogen.

Following the above studies on bi-layered ceramic membrane CGO/(CGO-GSFT), we further fabricated three-layered ceramic membrane CGO/(CGO-GSFT)/ p (CGO-GSFT) by introducing the porous support layer p (CGO-GSFT), which was then employed for upgrading the raw hydrogen. To accelerate the surface catalytic reactions, as shown in Figure S24, the three-layered membrane was coated by a porous $RuO_2@CGO$ on the CGO thin layer, and the backbone of its porous support layer was also infiltrated with Ru to catalyze water splitting. A gas mixture of 80 vol. % H_2O –20 vol. % He as the feed gas ($p_{H_2O} = 0.8 \text{ bar}$) and a simulated COG (composed of H_2 , CH_4 , N_2 and H_2S) as the sweep gas were injected on opposite sides of the membrane. As shown in Figure 4d, the H_2 production rate ($J(H_2)$) on the water-side increased gradually as the hydrogen concentration in the simulated COG stream was increased from 0 to 50 %. An H_2 production rate of

$1.84 \text{ cm}^3 \text{ min}^{-1} \text{ cm}^{-2}$ was achieved, which is higher than the production rate ($1.5 \text{ cm}^3 \text{ min}^{-1} \text{ cm}^{-2}$) reported recently using a proton ceramic electrolyzer,^[35] and is also comparable with those of many traditional oxygen permeable membrane reactors.^[34] Moreover, the $J(H_2)$ from water splitting can be increased further when increasing the operating temperature or the feed pressure of steam (Figures S25, S26). Figure 4e shows the effect of H_2S concentration in simulated COG on hydrogen production rate from water. When H_2S was introduced, the $J(H_2)$ decreased rapidly from 1.7 to $1.0 \text{ cm}^3 \text{ min}^{-1} \text{ cm}^{-2}$, which is probably caused by H_2S adsorption and the sulfidization of Ru in the catalytic layer.^[36] It then climbed gradually over the following 200 hours with increasing H_2S concentration, suggesting reconstruction of the Ru-containing catalytic layer in the H_2S -containing atmosphere.^[37] It can be finally recovered to its original value after shutting off the H_2S . The above results indicate that the three-layered ceramic membrane was robust for efficient and stable hydrogen production from water splitting assisted by COG oxidation.

Conclusion

A general, easily scalable and cost-competitive interface-reaction-induced reassembly approach was developed for the direct fabrication of zirconia- or ceria-based dense thin layers rooted in multilayered ceramic membranes by only one firing step from raw binary oxides. By deliberately applying a proper etchant Al_2O_3 , the surface Fe-containing grains in the dual-phase ceramic pellet were selectively etched *via* interface reactions at high temperatures, producing reaction enthalpy. The heat released by the interface reactions is expected to increase the local temperature for driving the reassembly of the surface isolated fluorite-type grains into a dense thin layer that cut off the interface reactions, avoiding the continuous growth of the thin layer. Thus, the resulting zirconia- or ceria-based layers are very thin ($\approx 1 \mu\text{m}$), highly dense and adhered strongly to the parent layers, not only significantly reducing the ionic transport resistance, but also ensuring the structural integrity of the multilayered membranes for various applications. When used as an oxygen permeable membrane for upgrading fossil-fuel-derived hydrogen, the multilayered membrane with a CGO dense thin layer shows very long durability (> 1000 hours) in harsh conditions containing H_2O , CH_4 , H_2 , CO_2 and H_2S , underscoring the promise of high-performance membrane reactors for hydrogen production in practical conditions. These results highlight the potential of the interface-reaction-induced reassembly approach to develop high-performance multilayered ceramics devices such as solid oxide cells, catalytic membrane reactors and gas sensors.

Acknowledgements

This work was supported by the National Key R&D Program of China (2022YFB3805503), the National Natural

Science Foundation of China (Grant Nos. 22178365, 22075306), the International Partnership Program of the Chinese Academy of Sciences (Grant No.153937-KYSB20180048), and Natural Science Foundation of Shandong Province (ZR2020ZD10). G.H. is grateful for support from the “Youth Innovation Promotion Association Chinese Academy of Sciences Grant 2018245”. The authors acknowledge Dr. Song Xue for the large-size sample preparation, Lidia Kibkalo for FIB preparation of the TEM specimen, and Prof. Xiaobo Yang for HT-XRD measurement.

Conflict of Interest

The authors declare no conflict of interest.

Data Availability Statement

The data that support the findings of this study are available from the corresponding author upon reasonable request.

Keywords: Hydrogen Production · Interface Reaction · Ion Conducting Thin Layer · Multilayered Ceramic Membrane · Oxygen Permeable Membrane

- [1] a) Z. Shao, S. M. Haile, J. Ahn, P. D. Ronney, Z. Zhan, S. A. Barnett, *Nature* **2005**, *435*, 795–798; b) W. Li, Z. Cao, L. Cai, L. Zhang, X. Zhu, W. Yang, *Energy Environ. Sci.* **2017**, *10*, 101–106.
- [2] E. D. Wachsman, K. T. Lee, *Science* **2011**, *334*, 935–939.
- [3] A. Hauch, R. Küngas, P. Blennow, A. B. Hansen, J. B. Hansen, B. V. Mathiesen, M. B. Mogensen, *Science* **2020**, *370*, eaba6118.
- [4] M. Li, H. Niu, J. Druce, H. Téllez, T. Ishihara, J. A. Kilner, H. Gasparyan, M. J. Pitcher, W. Xu, J. F. Shin, L. M. Daniels, L. A. H. Jones, V. R. Dhanak, D. Hu, M. Zanella, J. B. Claridge, M. J. Rosseinsky, *Adv. Mater.* **2020**, *32*, 1905200.
- [5] Y. Chen, B. deGlee, Y. Tang, Z. Wang, B. Zhao, Y. Wei, L. Zhang, S. Yoo, K. Pei, J. H. Kim, Y. Ding, P. Hu, F. F. Tao, M. Liu, *Nat. Energy* **2018**, *3*, 1042–1050.
- [6] K. Watanabe, M. Yuasa, T. Kida, Y. Teraoka, N. Yamazoe, K. Shimano, *Adv. Mater.* **2010**, *22*, 2367–2370.
- [7] a) S. Choi, C. J. Kucharczyk, Y. Liang, X. Zhang, I. Takeuchi, H.-I. Ji, S. M. Haile, *Nat. Energy* **2018**, *3*, 202–210; b) C. Duan, J. Tong, M. Shang, S. Nikodemski, M. Sanders, S. Ricote, A. Almansoori, R. O’Hayre, *Science* **2015**, *349*, 1321–1326; c) J. G. Lee, J. H. Park, Y. G. Shul, *Nat. Commun.* **2014**, *5*, 4045.
- [8] Y. Lyu, F. Wang, D. Wang, Z. Jin, *Mater. Tech.* **2020**, *35*, 212–227.
- [9] Y. Zhou, X. Guan, H. Zhou, K. Ramadoss, S. Adam, H. Liu, S. Lee, J. Shi, M. Tsuchiya, D. D. Fong, S. Ramanathan, *Nature* **2016**, *534*, 231–234.
- [10] a) H. An, H.-W. Lee, B.-K. Kim, J.-W. Son, K. J. Yoon, H. Kim, D. Shin, H.-I. Ji, J.-H. Lee, *Nat. Energy* **2018**, *3*, 870–875; b) A. Kaiser, S. Foghmoes, C. Chatzichristodoulou, M. Søggaard, J. A. Glasscock, H. L. Frandsen, P. V. Hendriksen, *J. Membr. Sci.* **2011**, *378*, 51–60.
- [11] S.-H. Lee, G. L. Messing, M. Awano, *J. Am. Ceram. Soc.* **2008**, *91*, 421–427.
- [12] P. I. Cowin, C. T. G. Petit, R. Lan, J. T. S. Irvine, S. Tao, *Adv. Energy Mater.* **2011**, *1*, 314–332.
- [13] F. Teocoli, D. W. Ni, S. Sanna, K. Thydén, F. C. Fonseca, V. Esposito, *J. Mater. Chem. A* **2015**, *3*, 17135–17143.
- [14] D. Wang, J. J. Tunney, X. Du, M. L. Post, R. Gauvin, *J. Appl. Phys.* **2008**, *104*, 023530.
- [15] Y. Chen, Y. Lin, Y. Zhang, S. Wang, D. Su, Z. Yang, M. Han, F. Chen, *Nano Energy* **2014**, *8*, 25–33.
- [16] a) M. S. Kabir, Z. Zhou, Z. Xie, P. Munroe, *Ceram. Int.* **2020**, *46*, 89–97; b) A. R. Phani, F. J. Gammel, T. Hack, H. Haefke, *Mater. Corros.* **2005**, *56*, 77–82.
- [17] H. J. Moon, S. Baumann, S. Uhlenbruck, D. Sebold, W. A. Meulenbergh, H. Park, *Thin Solid Films* **2012**, *526*, 59–64.
- [18] a) C. Fu, X. Ge, S. H. Chan, Q. Liu, *Fuel Cells* **2012**, *12*, 450–456; b) Y. Chen, Y. Zhang, J. Baker, P. Majumdar, Z. Yang, M. Han, F. Chen, *ACS Appl. Mater. Interfaces* **2014**, *6*, 5130–5136; c) J. Garcia-Fayos, M. Søggaard, A. Kaiser, J. M. Serra, *Sep. Purif. Technol.* **2019**, *216*, 58–64; d) D. Marani, V. Esposito, B. R. Sudireddy, J. J. Bentzen, P. S. Jørgensen, D. W. Ni, F. Teocoli, R. Kiebach, *Ceram. Int.* **2017**, *43*, 5647–5653; e) C. J. Fu, S. H. Chan, X. M. Ge, Q. L. Liu, G. Pasciak, *Int. J. Hydrogen Energy* **2011**, *36*, 13727–13734; f) S. Yoo, A. Jun, Y.-W. Ju, D. Odkhuu, J. Hyodo, H. Y. Jeong, N. Park, J. Shin, T. Ishihara, G. Kim, *Angew. Chem. Int. Ed.* **2014**, *53*, 13064–13067; *Angew. Chem.* **2014**, *126*, 13280–13283; g) L. Guesnet, J. M. Bassat, J. C. Grenier, T. Chartier, P. M. Geoffroy, *J. Eur. Ceram. Soc.* **2020**, *40*, 5662–5669; h) J. M. Serra, V. B. Vert, O. Büchler, W. A. Meulenbergh, H. P. Buchkremer, *Chem. Mater.* **2008**, *20*, 3867–3875; i) Y. D. Zhen, A. I. Y. Tok, S. P. Jiang, F. Y. C. Boey, *J. Power Sources* **2008**, *178*, 69–74; j) Q. L. Liu, S. H. Chan, C. J. Fu, G. Pasciak, *Electrochem. Commun.* **2009**, *11*, 871–874.
- [19] A.-R. Schulze, H. M. Buschbaum, *Z. Anorg. Allg. Chem.* **1981**, *475*, 205–210.
- [20] K. Kimura, M. Ohgaki, K. Tanaka, H. Morikawa, F. Marumo, *J. Solid State Chem.* **1990**, *87*, 186–194.
- [21] X.-L. Wang, C. R. Hubbard, K. B. Alexander, P. F. Becher, J. A. Fernandez-Baca, S. Spooner, *J. Am. Ceram. Soc.* **1994**, *77*, 1569–1575.
- [22] W. Xie, J. Quan, H. Wu, L. Shao, C. Zou, J. Zhang, X. Shi, Y. Wang, *J. Alloys Compd.* **2012**, *514*, 97–102.
- [23] H. Pausch, H. Müller-Buschbaum, *Z. Naturforsch. B* **1976**, *31*, 1148–1148.
- [24] L. Pastewka, M. O. Robbins, *Proc. Natl. Acad. Sci. USA* **2014**, *111*, 3298–3303.
- [25] H. Lin, E. V. Wagner, B. D. Freeman, L. G. Toy, R. P. Gupta, *Science* **2006**, *311*, 639–642.
- [26] L. Lei, F. Pan, A. Lindbråthen, X. Zhang, M. Hillestad, Y. Nie, L. Bai, X. He, M. D. Guiver, *Nat. Commun.* **2021**, *12*, 268.
- [27] a) L. Jia, G. He, Y. Zhang, J. Caro, H. Jiang, *Angew. Chem. Int. Ed.* **2021**, *60*, 5204–5208; *Angew. Chem.* **2021**, *133*, 5264–5268; b) X. Dong, W. Jin, N. Xu, K. Li, *Chem. Commun.* **2011**, *47*, 10886–10902.
- [28] G. Chen, A. Feldhoff, A. Weidenkaff, C. Li, S. Liu, X. Zhu, J. Sunarso, K. Huang, X.-Y. Wu, A. F. Ghoniem, W. Yang, J. Xue, H. Wang, Z. Shao, J. H. Duffy, K. S. Brinkman, X. Tan, Y. Zhang, H. Jiang, R. Costa, K. A. Friedrich, R. Kriegel, *Adv. Funct. Mater.* **2022**, *32*, 2105702.
- [29] J. Yi, M. Schroeder, M. Martin, *Chem. Mater.* **2013**, *25*, 815–817.
- [30] G. He, W. Liang, C.-L. Tsai, X. Xia, S. Baumann, H. Jiang, W. A. Meulenbergh, *iScience* **2019**, *19*, 955–964.
- [31] M. P. Lobera, J. M. Serra, S. P. Foghmoes, M. Søggaard, A. Kaiser, *J. Membr. Sci.* **2011**, *385*–386, 154–161.
- [32] H. Jiang, H. Wang, S. Werth, T. Schiestel, J. Caro, *Angew. Chem. Int. Ed.* **2008**, *47*, 9341–9344; *Angew. Chem.* **2008**, *120*, 9481–9484.

- [33] Y. Liu, X. Zhu, M. Li, H. Liu, Y. Cong, W. Yang, *Angew. Chem. Int. Ed.* **2013**, *52*, 3232–3236; *Angew. Chem.* **2013**, *125*, 3314–3318.
- [34] R. Kiebach, S. Pirou, L. Martinez Aguilera, A. B. Haugen, A. Kaiser, P. V. Hendriksen, M. Balaguer, J. García-Fayos, J. M. Serra, F. Schulze-Küppers, M. Christie, L. Fischer, W. A. Meulenberg, S. Baumann, *J. Mater. Chem. A* **2022**, *10*, 2152–2195.
- [35] E. Vøllestad, R. Strandbakke, M. Tarach, D. Catalán-Martínez, M.-L. Fontaine, D. Beeaff, D. R. Clark, J. M. Serra, T. Norby, *Nat. Mater.* **2019**, *18*, 752–759.
- [36] R. A. Cocco, B. J. Tatarchuk, *Langmuir* **1989**, *5*, 1309–1315.
- [37] Q. Zhu, S. L. Wegener, C. Xie, O. Uche, M. Neurock, T. J. Marks, *Nat. Chem.* **2013**, *5*, 104–109.

Manuscript received: July 18, 2022

Accepted manuscript online: November 3, 2022

Version of record online: November 24, 2022